RSC Advances

This is an *Accepted Manuscript*, which has been through the Royal Society of Chemistry peer review process and has been accepted for publication.

Accepted Manuscripts are published online shortly after acceptance, before technical editing, formatting and proof reading. Using this free service, authors can make their results available to the community, in citable form, before we publish the edited article. This *Accepted Manuscript* will be replaced by the edited, formatted and paginated article as soon as this is available.

You can find more information about *Accepted Manuscripts* in the Information for Authors.

Please note that technical editing may introduce minor changes to the text and/or graphics, which may alter content. The journal's standard Terms & Conditions and the Ethical guidelines still apply. In no event shall the Royal Society of Chemistry be held responsible for any errors or omissions in this *Accepted Manuscript* or any consequences arising from the use of any information it contains.

ROYAL SOCIETY OF CHEMISTRY

www.rsc.org/advances

The hierarchical porosity of three-dimensional graphene electrode for binder-free and high performance supercapacitors

Jun-He Chang [†#], Yu-Han Hung[†#], Xu-Feng Luo[%],Chi-Hsien Huang [$], Sungmi Jung[^], Jeng-Kuei Chang[%] ,Jing Kong[^] and Ching-Yuan Su [†#]*

[#] *Graduate Institute of Energy Engineering, National Central University, Tao-Yuan 32001 , Taiwan*

[†] *Dep. of Mechanical Engineering, National Central University, Tao-Yuan 32001 , Taiwan*

[$] *Dep. of Materials Engineering, Ming Chi University of Technology,New Taipei City 24301, Taiwan*

[%] *Graduate Institute of Material Science and Engineering, National Central University, Tao-Yuan 32001 , Taiwan*

[^] *Department of Electrical Engineering and Computer Sciences, Massachusetts Institute of Technology, 77 Massachusetts Avenue, Cambridge, MA 02139, USA*

To whom correspondence should be addressed: (C. Y. Su) : cysu@ncu.edu.tw

KEYWORDS: Graphene, Supercapacitors, Energy storage

Abstract

In this study, we report a binder-free supercapacitor including a unique graphene electrode of hierarchical porosity composed of the submicrometer porosity(~20 μm) of 3D graphene self-assembled by nanopores(~2.5 nm)of graphene flakes. The hierarchical 3D porosity of the graphene electrode was prepared by a facile and scalable approach

RSC Advances Accepted Manuscript

based on acid activation and freeze-drying. Remarkably, we found that this unique graphene-based electrode, when used in a supercapacitor, shows improved performance compared with a reported graphene electrode; these improvements include high specific capacitance(~442 F/g), fast rate charging/discharging, and excellent cycle stability(95% after 1600 cycle numbers), which were due to (1) the creation of a high specific surface area and a diffusion path, thus promoting ion transport capability, and (2) the additional pseudocapacitor due to the controlled oxygen amount of functionalization on the graphene surface. The resultant device shows an energy density of 51.9 Wh/kg and a power density of 467.8 W/kg. This study introduces a new concept for the binder-free, cost-effective and high performance of a graphene-based supercapacitor, which could pave the way for practical applications in frontier energy devices.

. Introduction

Graphene-based electrical energy storage devices, such as Li-ion batteries(LIBs) and supercapacitors, have attracted intensive attention in recent years due to their unique characteristics of high specific capacitance, long cycling stability and excellent mechanical flexibility.[1-5] In particular, supercapacitors show rapid charge/discharge storage mechanisms and a higher power density than LIBs, enabling supercapacitors to be potential applied in portable electronics and hybrid electric vehicles. Currently, supercapacitor technology is subdivided into two classes: electrochemical double-layer capacitors (EDLCs) and pseudocapacitors.[6, 7] The EDLCs are based on reversible ion adsorption on the interface of the electrode and electrolyte when subjected to a voltage bias.[8] Therefore, for the supercapacitor, the formation of an available high surface area on the electrode can significantly increase the amount of charge storage per unit mass (F /g). The recent works using graphene as the EDLC electrode material were mainly due

RSC Advances Accepted Manuscript

to its excellent electrical conductivity, ultrahigh specific surface area(SSA) and chemical stability.[7, 9-11] The theoretical SSA in graphene is 2675 m^2/g, and the capacitance is estimated to be 550 F/g.[6, 7] To achieve the requirements of energy devices, it has been reported that the efficient ionic and electron transport kinetics are key for the high density and high performance of a supercapacitor.[12] However, recent works involving reduced graphene oxide (rGO-derived) or graphene flakes as electrodes show lower ion diffusion due to the parallel restacking of two-dimensional graphene sheets when they were assembled into electrodes; thus, the restacking significantly degrades the specific surface area.[13, 14] Recent reports demonstrate the construction of macroscopic three-dimensional(3D) bulk assemblies of graphene with an enhanced high SSA for versatile applications. These 3D frameworks can be produced via chemical vapor deposition(CVD) over catalytic metal foam or via self-gelation from the bottom-up assembly of GO or graphene flakes.[15-21] The porosity is over the microscale range of ~20 μm to 70 μm. Recent reports show that the graphene-based monoliths exhibit ultralow density, high elasticity and electrical conductivity and thus show potential especially for the hybrid electrode in energy storage applications.[22] To date, numerous reports have studied hybrid electrodes for use in energy storage by constructing 3D porous frameworks for increasing the SSA and ion and electron transport. [15, 23-26] Tao et al., reported the ultrahigh volumetric capacitance of up to 376 F/cm^3 by altering porous structured graphene as an electrode in an aqueous electrolyte(KOH). More importantly, the assembly of a porous graphene electrode in a supercapacitor led to a binder-free electrode without any additives, resulting in a high energy density storage device that can be used in practice. [27] Zhu et al. reported the first work on the electrochemical capacitance of 3D graphene with an ionic liquid electrolyte($EMIMBF_4$/ AN), resulting

RSC Advances Accepted Manuscript

in a high energy density of ~68 Wh/kg.[28] Zhang et al. demonstrated the unique performance of high ion and electron transportation of graphene hydrogels for supercapacitors with high rate capability, where the reduced graphene electrode exhibited a high specific capacitance of 220 F/g at 1A/g, and it maintained 74% of the capacitance for high rate discharging up to 100 A/g, thus making it promising for high rate charge/discharge devices. [29]As for the solid-state supercapacitors, Xu et al. reported the fabrication of a flexible solid-state supercapacitor based on a 3D macroporous graphene electrode by utilizing H_2SO_4-polyvinyl alcohol(PVA) as a gel electrolyte, exhibiting a gravimetric specific capacitance of 196 F/g. Moreover, the excellent cycling stability and mechanical flexibility highlight the potential of such a supercapacitor for use as a high performance flexible energy storage device. In addition, Zhu et al. reported that the 3D graphene structure decorated with metal oxide as a hybrid electrode (3D graphene/CoO nanorod) is able to take advantage of both EDLCs and pseudocapacitors for energy storage, where the 3D graphene was employed as a conductive supporting electrode with a large number of host sites for the pseudocapacitive active material of cobalt oxide. [30] The hybrid electrode achieved an extremely high capacitance of ~ 600 F/g at 20 A/g.

Compared with the 3D macroporous graphene structure, an alternative approach to increase the SSA of a graphene electrode is to create nanopores on the graphene basal plane. Such a mesoporous holey graphene structure can be prepared in a facile manner by the traditional activation procedure. The well-known approach is KOH activation for carbon materials, including activated carbons and carbon nanotubes or fibers as well as graphene nanosheets.[31] Such activated carbon materials have been regarded as potential

RSC Advances Accepted Manuscript

materials for electrochemical energy systems.[32] In 2011, Zhu et al. employed KOH activation of exfoliated graphene sheets to create nanopores(primarily 0.6~5 nanometer pores) on sp^2 carbon networks, resulting in a superior high SSA of up to 3200 m^2/g.[11] The constructed electrode in a supercapacitor yielded a high gravimetric capacitance of 166 F/g in the electrolyte of 1-Butyl-3-methylimidazoliumtetrafluoroborate(BMIM BF_4/AN) at a constant current of 5.7 A/g and a working voltage of 3.5 V. The energy density and power density were70 Wh/kg and 250 kW/kg, respectively. In 2013, Zhang et al. demonstrated a hydrothermal carbonization process on a GO and sucrose mixture, followed by KOH activation. The as-prepared graphene porous materials with pore size distributed from 0.5~5 nm exhibited an ultrahigh SSA of 3523 m^2/g. The resultant specific capacitance and energy density based on this electrode were 231 F/g and 98 Wh/kg, respectively.[33] Zhao et al. reported another activation process to obtain a cleaner nanoporous graphene product, by using HNO_3 as reactive agents, comprising sonication to generate in-plane porosity on graphene sheets, followed by thermal reduction to complete the process[34]; the LIBs made by these materials show excellent high-rate Li-ion storage capabilities due to the enhanced ion diffusion kinetics.

The aforementioned concept with the 3D graphene macroporous structure and the 2D holey graphene structure can both significantly increase the SSA on the bulk scale, resulting in the excellent energy storage performance of the graphene-based supercapacitor. However, there is still a lack of reports on combining both of these two structures as an electrode for use in energy storage. This knowledge gap motivated this work, where the microporous 3D graphene scaffold provides an interconnected conductive electrode for ion permeation, while the assembly of nanoporous holey

RSC Advances Accepted Manuscript

graphene creates another set of ion diffusion paths for propagation through these 3D graphene electrodes.

Here, we fabricate and characterize a binder-free graphene-based supercapacitor integrated with 3D self-assembled nanoporous graphene as a hybrid electrode by facile approaches of activation and freeze-drying. The as-prepared functionalized electrode exhibit a SSA of up to 564 m^2/g. The optimized condition allows us to yield an average capacitances of 364 F g^{-1} and highest specific capacitances of ~442 F/g at a rate of 2 A/ g. The energy density and power density are 51.9 Wh/kg and 467.8 W/kg, respectively. Moreover, the superior cycling stability and rate capabilities suggest the high ion permeance and high electronic conductivity of this unique and multifunctional graphene electrode. The reported approach is facile, scalable and cost-effective, which is promising for the production of high performance graphene-based energy storage devices.

Results and Discussion

In this work, the starting material was graphene oxide(GO), which was prepared by the improved Hummers' methods(see the experimental section for details). Figure 1 shows the morphology of as-prepared GO flakes. **Figures 1 a,b** show the typical AFM image and the height profile, revealing flakes with sizes of up to 45 μm and a typical thickness of 1.02 nm. **Figures 1c,d** show SEM and TEM images, which display the clean surface and the wrinkled structure on the basal plane of a graphene flake, implying that high-purity thin-layered flakes were obtained. To construct the 3D bulk electrode self-assembled nanoporous graphene, the process comprises three steps, as

RSC Advances Accepted Manuscript

illustrated in **Figure 2a**: (1) creation of nanopores on GO through an activation process; (2) self-assembly of the 3D graphene monolith by freeze-drying; and (3) thermal reduction of 3D graphene. **Figure 2b** shows the photo images for the as-prepared GO 3D monolith and the corresponding reduced graphene electrode, where the monolithic size can be adjusted by tailoring the initial mode. The reduced graphene monolith shows mechanical elasticity and compressibility**(see the supporting movie clip)**, which is beneficial for a durable electrode in an energy storage device. **Figure 2c** shows SEM images for the microstructure of a 3D graphene monolith, exhibiting the interconnected graphene with the porous network. The pore size ranged from a few micrometers to tens of micrometers, and the average value was approximately 20 μm, as revealed in the magnified image. Moreover, to create the nanopores on the graphene flakes(i.e., holey graphene), the activation process is carried out according to a facile method using a mixture of GO solution with 70% concentrated HNO_3 under water-based sonication.[35, 36] During the process, the induced high strain from the cavitation bubbles by the acoustic pressure creates a scission force on the graphene basal plane and then breaks the carbon framework. Next, the HNO_3 reacts with these defect sites on the edges, resulting in the removal of carbon atoms from the GO flakes. **Figures 2d,e** show typical TEM images for the pristine GO and the activated GO sheets. The image for the GO after the activation treatment reveal large amounts of highly dense nanopores over the entire basal plane of the GO flake(**Figure2e**), in clear contrast to the control sample of pristine GO flakes(**Figure2d**). To verify the mesoporous structure of the active graphene, N_2 adsorption-desorption analysis was performed. Figure 2f shows the highest pore volume with the pore size ranging from 2.0~4.5 nm, primarily at ~2.14 nm. The pore size distribution was consistent with the statistically estimated nanopore size

RSC Advances Accepted Manuscript

distribution from the high magnified HRTEM observation(**see Figure S1**). The results imply the efficient formation of holey graphene by such an acid treatment. It has been reported that the degree of reduction conditions significantly affect the surface chemical and physical properties, such as electrolyte wetting, charge transferring and electrical conductivity, due to the complex composition of oxidized functional groups, resulting in different electrochemical performance.[37, 38] In addition, the proposed nanoporous graphene during the activation procedure and the 3D structure might affect these properties. To study in detail the effects of the 3D structure and surface chemistry properties on the electrochemical performances, several samples were prepared with various conditions, including different annealing temperatures (arranged from 400~800 ^{o}C) and different structured graphene (see excremental section for the sample definitions and detail conditions)

Figure 3a shows the XPS C1s spectra and the corresponding deconvoluted peaks on samples produced via thermal reduction or samples produced by the combination of activation and thermal reduction at various temperatures. The oxidized functional groups on the in-plane graphene were mainly C-O, C=O, and O-C=O, centered at 286.7, 287.8, and 288.9 eV, respectively. The integrated areas of deconvoluted peaks from C1s bonding states are plotted in **Figure 3b,** and the values are listed in **Table1**. The C/O ratio clearly increased with increased reduction temperature due to the effective removal of oxidized groups, especially the reduction of C-O bonds. Moreover, the C/O ratio clearly decreased and the C=O and O-C=O components became more prominent when the GO was subjected to the activation procedures. In addition, the C-O shows lower intensity for the nanoporous graphene after the activation treatment. This result indicates the enrichment of C=O and O-C=O groups on the as-prepared holey graphene.

RSC Advances Accepted Manuscript

This result is also consistent with the activated carbon materials in reported works.[34] The same features can also been distinguished from the phonon mode of the Raman spectra, as shown in **Figure 3c**, where the integrated area intensity ratio of the D peak to G peak (I(D)/I(G)) is slightly increased when the sample was treated with HNO_3 activation. The results suggest a higher defect degree arising from large amounts of edge states on the basal plane of holey graphene flakes.

To investigate the influence of different graphene structures on the electrochemical performance, the three-electrode testing system with the electrolyte of KOH aqueous solution was used (see **Figure S2** for details on the setup). The testing electrodes composed of graphene materials were prepared by supporting graphene in a Ni foam, followed by the direct thermal drying or freeze-drying procedures; the photo images and SEM images are shown in **Figure S3**. The results show that the graphene flakes spontaneously crumpled and restacked over the surface of the Ni ligaments following the direct thermal drying process, while the 3D porosity graphene could be retained among the Ni foam without restacking following the freeze-drying process. Herein, the Ni foam supporting the electrode was found to load graphene uniformly; however, Ni might be expected to participate in the electrochemical reaction during the measurements. Nevertheless, the cyclic voltammetry(CV) curves in **Figure S4** revealed a negligible capacitance contribution from the pristine Ni foam compared with the graphene samples, indicating that it is appropriate to hybridize graphene with the Ni foam as a binder-free electrode. Moreover, there were no apparent phenomena of the peel–off of graphene from the electrode when the electrode was subjected to a 2000-cycle test, suggesting the mechanical strength and operational reliability of the as-

RSC Advances Accepted Manuscript

prepared graphene hybrid electrode ((c) in Figure S2).**Figure 4a** shows the compiled CV curves for different structured graphene samples under thermal reduction at 400°C, where all the CV curves exhibit a quasi-rectangular shape(other CV curves with different temperatures are also shown in **Figure S5**), indicating a nearly ideal supercapacitive characteristic. Compared with all the curves, the 3D self-assembly of graphene(FG 400) shows higher capacitance than that of restacked holey graphene(AG400), suggesting that the macroporous structure dominates the ion propagation more efficiently than the nanoporous structure. Moreover, the 3D self-assembly of holey graphene(FAG400) shows superior high performance than other conditions, suggesting that the hierarchical porosity of the 3D monolith assembled from holey graphene, especially its macroporous structure, dominates and enhances the capacitive performance. Note that the curve from FAG 400 shows apparent redox peaks, indicating the additional contributions of pseudocapacitance beside the EDLC, which is mainly attributed to the larger amount of oxygen groups on graphene at a lower reduction temperature (see the C/O ratio in **Table1**). In addition, FAG 400 shows more clear redox peaks than AG400, revealing the existence of many oxygen-functional groups exposed to react with the ion electrolyte due to the increase of the more accessible surface area created in the macroporous structure.

In this work, the FAG sample always shows higher performance than the other samples. Taking FAG 400 as an example, **Figure 4b** shows typical CV curves for FAG 400 at various scan rates; the current response increases accordingly with an increase in scan rate from 5 mV/s to 200 mV/s, and the CV curves maintain their rectangular shape without severe distortions, implying the excellent rate performance and low internal resistance. **Figure 4c** shows the galvanostatic charge-discharge(GCD) curves for

RSC Advances Accepted Manuscript

FAG400 at different current densities, where the nearly symmetric triangle curves were observed for the current densities ranging from 2A/g to 20A/g, consistent with EDLC features. The specific capacitance is calculated to be 442 F/g at 2 A/g, which is superior to that for the other conditions shown here and is comparable to the best performance of graphene-based supercapacitors. Moreover, from the GCD curve (**Figure 4d**), FAG 400 shows a smaller voltage IR drop(1.6 mV) than FG 400(3.4 mV), AG400(11.1 mV) and G400(34.1 mV), indicating the lower equivalent series resistance(ESR) for FAG 400. Furthermore, **Figure 4e** shows the tests for the cycling stability; FAG400 could retain 95% of the initial capacitance over 1600 cycles, indicating excellent cycling stability at a high current scan rate of 200 mV/s. The above discussions demonstrate that the tailored graphene electrodes made from various structures highly affect the supercapacitor performances, suggesting that the high accessible surface area in FAG samples promotes the ion diffusion dynamic along both the macropores and the nanopores of the graphene electrode. To verify this suggestion, the specific surface area(SSA) values were estimated on different structured graphene electrodes by methylene blue (MB) dye adsorption methods(see the experimental section). **Figure 4f** reveals that the FAG samples shows SSA of ~564 m^2/g, which is ~48% higher than that of the restacking graphene electrode(G400 ~ 381 m^2/g), indicating that the combination of the macroporous structure of the 3D monolith and the nanopores on the holey graphene sheets could highly increase the SSA and thus create many ion permeation and diffusion paths(as illustrated in the inset of **Figure 4f** and additional N_2 adsorption–desorption isotherms characterization can be referred to **Figure S10**).

RSC Advances Accepted Manuscript

In addition to the effect of the micro/nanostructures, the samples at different reduction temperatures also reveal variations in their electrochemical properties. **Figure 5a** shows the compiled CV curves for the FAG samples with different thermal reduction temperatures of 400, 600, and 800 °C. Note that the samples with higher temperature treatment show a decayed capacitance over all structure conditions(i.e., G, AG, FG, and FAG samples), which could be attributed to two main reasons:(1) the decrease of the interlayer spacing and(2) the loss of oxidized-functional groups. Previous reports have shown that the interlayer spacing of stacking graphene gradually decreased from 3.78 Å to 3.37 Å when it was reduced at temperatures from 200 to 900°C due to the removal of oxygen-containing functional groups between the graphene interlayer.[39] The decrease of the interlayer spacing lowers the accessible passage for ions diffusing to the interior graphene surface and thus degrades its charging/discharging process. The second reason for the decayed capacitance at higher temperature is the loss of most oxidized functional groups on the graphene surface, as shown in Figure 3(a), because these functional groups were regarded as facilitating the redox process on the graphene surface, which could provide the additional effect of pseudocapacitance.[40] However, the existence of functional groups on graphene also helps to enhance the wettability, and this wettability could highly improve the ionic accessibility between the electrolyte and electrode.[26, 41]**Figure S6** shows that the contact angle increases from 73^{o} to 88^{o}with increasing reduction temperature from 400 to 800°C, indicating the higher wettability of graphene with the electrolyte at lower temperature reduction. Therefore, the partial removal of oxidized functional groups from the graphene surface by moderate reduction of GO results in suitable surface chemistry properties for obtaining higher ionic propagation capability. To study the details of the optimized conditions for the graphene electrodes,

RSC Advances Accepted Manuscript

the additional conditions of thermal reduction at 300°C (FAG300) and 500°C(FAG 500) were studied(see **Figure S7**). When the temperature is lower than 400°C(FAG 300), the electric conductivity was apparently degraded, resulting in a lower capacitance of 197 F/g due to the higher internal series resistance. Herein, the voltage IR drops were probed to study the series resistance, as shown in **Figure 5b**, where FAG 400 reveals an unexpected smaller IR drop(7.1 mV) than that of FAG 600(49.8 mV) and FAG 800(89.1 mV), suggesting the lower equivalent series resistance for 400°C reduction. To further understand the rate performance and the ion diffusion kinetics of the FAG samples, electrochemical impedance spectroscopy (EIS) was used in this study. **Figure 5c** shows the Nyquist plot taken from 10^{6} Hz to 0.1 Hz. In the low frequency regime, the nearly vertical line indicates the pure capacitive behaviors of FAG 400. In the high frequency regime(the inset in **Figure 5c**), the Nyquist plot reveals a smaller diameter of the semicircle for FAG 400 than for the others, confirming the lower charge transfer resistance and highly efficient ion diffusion within such hierarchical porosity structures of the FAG samples. In addition, the nearly 45^{o} angle in the Warburg region is a typical characteristic for an electrolyte permeated and saturated within a porous electrode.[42] Moreover, the x-intercept of the Nyquist plot has been reported to probe the equivalent series resistance(ESR) of the electrode. In this work, FAG 400 shows a smaller x-intercept value of ~0.59 Ω than FAG 600 (0.71 Ω) and FAG 800 (0.86 Ω), implying the relatively small ESR, which is attributed to the shortened ion diffusion paths in the unique hierarchical porosity of the FAG structure, as shown in the inset of **Figure 4f.** **Figure 5d** shows the rate capacitances for the FAG samples, including for FAG 400, where the electrode exhibited the specific capacitance of 247 F/g and 188 F/g as the current density increased from 2 to 20 A/g (maintaining 76% of the specific

RSC Advances Accepted Manuscript

capacitance), indicating the high rate properties. Note that the lower capacitance shown here compared with the capacitance obtained from the CV curve(**Figure 5e**) is mainly due to the different scan rate(see **Figure S8** for details). The high rate performance is enabled by the fast charge transfer of the high conductivity graphene electrode, resulting in an excellent discharge process at high current density.[43]

Figure 5e plots the histograms for the compiled specific capacitance for all the studied graphene-based electrodes. The result clearly shows that FAG 400 allows for obtaining the average capacitance of 384 F/g (corresponding to an areal capacitance of 0.66 F/m^2), with the highest capacitance being up to ~442 F/g. This value is also superior to most of those in the reported works on graphene-based supercapacitors(as listed in **Table S1**). From the view point of the electrode structure, the hierarchical porosity of the FAG samples comprises macropores and nanopores in the graphene monolith, which provide the most efficient ion diffusion process. However, the moderate thermal reduction temperature results in the excellent surface chemistry and electrical conductivity of the graphene electrode. The partial removal of the oxygen-functional groups on the graphene surface not only retains the larger interlayer spacing(i.e., high SSA), which is beneficial for ion transport, but also provides the additional pseudocapacitance properties in addition to the EDLC. Thus, the capacitance comprising these factors significantly promotes the capacitance performances. To evaluate the capacitance on graphene-based electrodes, the Ragone plots(the energy density (E) vs. power density(P)) are shown in **Figure 5d**. The results indicate that FAG 400 shows an energy density of 51.9 Wh/kg and a power density of 467.8 W/kg, which is significantly higher than that of the other conditions we studied here. Moreover, The device shows a energy

RSC Advances Accepted Manuscript

density of 12.98 Wh/kg and power density of 116.88 W/kg for a symmetric two-electrode system. **Figure S9** and **S10** summarize the Ragone plots of this work compared to previous studies on supercapacitors with 3D graphene electrodes. The proposed hierarchical porosity of the graphene electrode demonstrated a high SSA and excellent electrical and ionic conductivity, making it promising for high performance supercapacitors in the future.

4. Conclusion

In conclusion, a graphene electrode of unique hierarchical porosity characterized by the submicrometer porosity of 3D graphene, self-assembled by nanopore graphene flakes, was prepared by a facile and scalable approach based on acid activation and freeze-drying. The graphene electrode shows a superior high specific surface area of up to 564 m^2/g, which is ~48% higher than that of a restacking graphene electrode obtained by direct thermal drying. The ultrahigh SSA thus effectively enhances the ionic diffusion capability. In addition, the graphene electrode with moderate reduction of 400°C retains partial oxidized functional groups, which is beneficial for the electrolyte wettability and the contribution of an additional pseudosupercapacitor. The supercapacitors integrating such unique hierarchical porosity of the graphene electrode demonstrate high specific capacitance upto ~442 F/g, excellent rate performance and cycling stability. The device shows an energy density of 51.9 Wh/kg and a power density of 467.8 W/kg. This work introduces a new concept of binder-free, cost-effective and high performance graphene-based supercapacitors that pave the way for practical applications in frontier energy devices.

Experimental Section*:*

RSC Advances Accepted Manuscript

Synthesis of graphene oxide (GO)

For preparing graphene oxide, the basic process is a modified Hummers' method.[44] In this present method, graphite powder (Chuetsu Graphite Works Co.,Ltd.; 20 mesh) was employed as the starting materials for producing graphene oxide. The graphite powder (3 g) was mixed with the mixture solution of 96% H_2SO_4 and 85% H_3PO_4 (3:1 in 400 mL). Next, $KMnO_4$ (18 g)was added to the solution, followed by stirring in an ice-bath for 10 min. The solution was then heated to 50°C and stirred for 18 hr. Afterward, the solution was diluted with 400 mL of DI water. Shortly thereafter, 15 mL of H_2O_2(30%) was poured into the mixture. The color suddenly changed to bright yellow. We then collected the upper portions of the solution because unreacted graphite particles are precipitated in the bottom of the solution. The obtained solution was centrifuged at 9000 rpm and dissolved in a 1:10 HCl solution to remove the residual metal ions. Finally, the product was subjected to a repeated process to remove the acid by dissolving it in DI water and then centrifuging it until the pH of the solutionwas close to 7.0.

Synthesis of activated GO, reduction and electrode fabrication:

A total of 30 mL of the prepared GO solution(10 mg/mL in DI water) was mixed with 70% concentrated HNO_3 in the amount of 360 mL and then sealed in a 500 mL glass vial under stirring for 1 min. The mixed solution was then sonicated in a water bath sonicator for 1 hr, followed by replacement of the solvent with DI water by adding water and centrifuging until a neutral pH of 7 was obtained.

To prepare the graphene electrode in the supercapacitor device, 0.8-1.5 mg of graphene was loaded into a Ni-foam electrode. Prior to the process, the organic impurity on the Ni-foam surface must be removed by a thermal treatment in a furnace under a mixture gas of H_2/Ar (20/80 sccm) at 1000°C for 30 min. Next, the Ni foam was immersed in the GO aqueous solution (the optimized concentration is 10 mg/mL in regards to the

RSC Advances Accepted Manuscript

mechanical strength of the graphene monolith), followed by bath sonication for 30 min. This process allows graphene flakes to easily permeate into the macropores in the Ni foam. There are two drying routes to obtain the graphene electrodes: (1) direct drying, where the gelation formation occurred during thermal drying at 80°C for 30 min, and the material was then fully dried for further backing in an oven for 6 hr; (2) freeze drying, where the GO loaded Ni foam was frozen by liquid nitrogen, and it was then placed into a freeze dryer chamber, followed by sublimation of the resulting solid ice under a pressure of 1×10^{-3} Torr for 24 hr.

Before the integration of the graphene electrode into a device, an additional thermal reduction at various temperatures(400 °C, 600 °C, and 800°C) was employed to study the effect of the degree of surface oxidations. The reduction process in a furnace is typically performed under a mixture gas of H_2/Ar (20/80 sccm) for 30 min.

All samples with various conditions were prepared and labelled as below: (1) stacking reduced GO with direct drying at different annealing temperatures of 400°C, 600°C, and 800°C (defined as G400, G600, and G800,respectively); (2) stacking reduced and activated GO at annealing temperatures of 400°C, 600°C, and 800 °C(defined as AG400, AG600, and AG800,respectively); (3) free-standing 3D structured and reduced graphene at different annealing temperatures of 400°C,600°C,and 800°C(defined as FG400, FG600, and FG800,respectively); and (4) free-standing, activated and reduced 3D graphene at different annealing temperatures of 400 °C,600 °C, and 800°C(defined as FAG400, FAG600, and FAG800,respectively).

Material characterizations:

AFM images were obtained using a Veeco Dimention-Icon system to characterize the thickness of the as-prepared GO flake. Raman scattering spectra were collected using a

RSC Advances Accepted Manuscript

Horiba HR 550 confocal Raman microscope system (laser excitation wavelength = 532 nm; laser spot-size ~ 0.5 μm). The Raman scattering peak of Si at 520 cm^{-1} was used as a reference for wavenumber calibration. The chemical configurations were determined using an X-ray photoelectron spectrometer (XPS, Phi V6000). The XPS measurements were performed using a Mg-Kα X-ray source for sample excitation. The energies were calibrated relative to the C1s peak(at about 284.8 eV) to eliminate the charging of the sample during analysis. The deconvolution and curve fitting were performed as followed steps: (1) Select Gaussian-Lorentzian function for the fitting procedure.(2) Add the selected peaks according to the XPS bonding status: C-O(at 286.7 eV), C=O(287.8 eV), O-C=O(288.9eV).(3) Constrain full width at half maximum (FWHM) to be equal to each other for all peaks. The SEM images were obtained in a JEOL-6330F instrument, and the TEM observations were performed in a JEOL-2010F with an accelerating voltage of 200keV. The electrical conductivity measurements were performed on a four-point-probe system(FPSR100). The specific surface area(SSA) was characterized using the methyl blue dye adsorption method.[45] First, the mass of the graphene sample was measured. MB powder was added to absolute alcohol as a solvent until it reached saturation, followed by ultrasonication for 30 min to ensure good dispersion. Violate alcohol was then removed by vacuum drying in the oven for 2 hr. The amount of absorbed MB was determined by calculating the difference of the sample before and after the immersion of MB solution; note that the amount of Ni foam was subtracted in the calculation. For the estimation of the SSA, 2.54 m^2 of the surface covered per mg of MB adsorbed was the basis in this work. The pore size distribution and SSAs were determined by the N_2 adsorption–desorption isotherms analysis, where

RSC Advances Accepted Manuscript

the porosities of the graphene electrode were measured on a Micromeritics ASAP 2020 system.

Electrochemical characterizations for supercapacitor devices:

The electrochemical testing was performed using a standard three-electrode setup in an electrochemical workstation (Biologic; SP-150) composed of a Pt wire as the counter electrode, AgCl/Ag as the reference electrode, and 6 M KOH aqueous solution as the electrolyte. The cyclic voltammetry (CV) measurements were performed at 5, 20,50, 100, 200, 500 and 1000 mV/s between a potential in the range from 0 and -1 V. Note that the effective CV data discussed here were acquired after three cycles to ensure the variations during the testing (Figure S2(b)). The galvanostatic charge/discharge (GCD)cycle tests were performed in an Arbin system in the voltage range of -1~0 V at various current densities of 0.1 A/g, 5 A/g, and 20 A/g. The electrochemical impedance spectra (EIS) measurement was employed (Biologic; VSP-300)with an amplitude of 10 mV from 10^{6} Hz to 0.1 Hz. The energy density and power density in the Ragone plots were calculated from the GCD curves on a single-electrode supercapacitor according to the equations of $E= CV^2/2$ and $P=QV/2t=E/t$, where E, C,V,Q, t and P are the energy density, specific capacitance per unit mass, discharge potential windows, total delivered charges, discharge time, and average power density, respectively.

Acknowledgments: This research was supported by National Science Council Taiwan (102-2221-E-008-113-MY3).

RSC Advances Accepted Manuscript

Supporting Information Available: The detailed characterizations, such as SEM, contact angle, HRTEM, and electrochemical measurements, are available free of charge via the Internet at http://pubs.acs.org

Tables

Table 1. The calculated C/O ratio, composition of various bonding states(from C1s inXPS) and the feature peak ratios from Raman spectra for reduced graphene and activated graphene.

		C 1s XPS peak area ratio(%)				Raman
Sample	**C/O ratio**	**C-C**	**C-O**	**C=O**	**O-C=O**	**ID/IG**
G400	7.5	74.89	17.57	4.81	2.73	1.39
AG400	3.9	72.23	19.33	5.03	3.41	1.34
G600	8.1	76.63	15.80	4.55	3.02	1.39
AG600	6.5	75.54	15.47	5.76	3.24	1.43
G800	15.7	80.52	14.70	3.84	0.95	1.48
AG800	14.8	79.65	14.14	4.42	1.80	1.59

RSC Advances Accepted Manuscript

Table 2. The specific surface area(SSA) for various samples estimated by the MB dye adsorption method.

sample	**Before absorption(mg)**	**After(mg)**	**Uptake(mg)**	**Estimated SSA(m^2/g)**
FAG400	2.6	3.3	0.7	564
FG400	3.5	4.2	0.7	508
AG400	1.7	2	0.3	448
G400	2	2.3	0.3	381

RSC Advances Accepted Manuscript

Figures

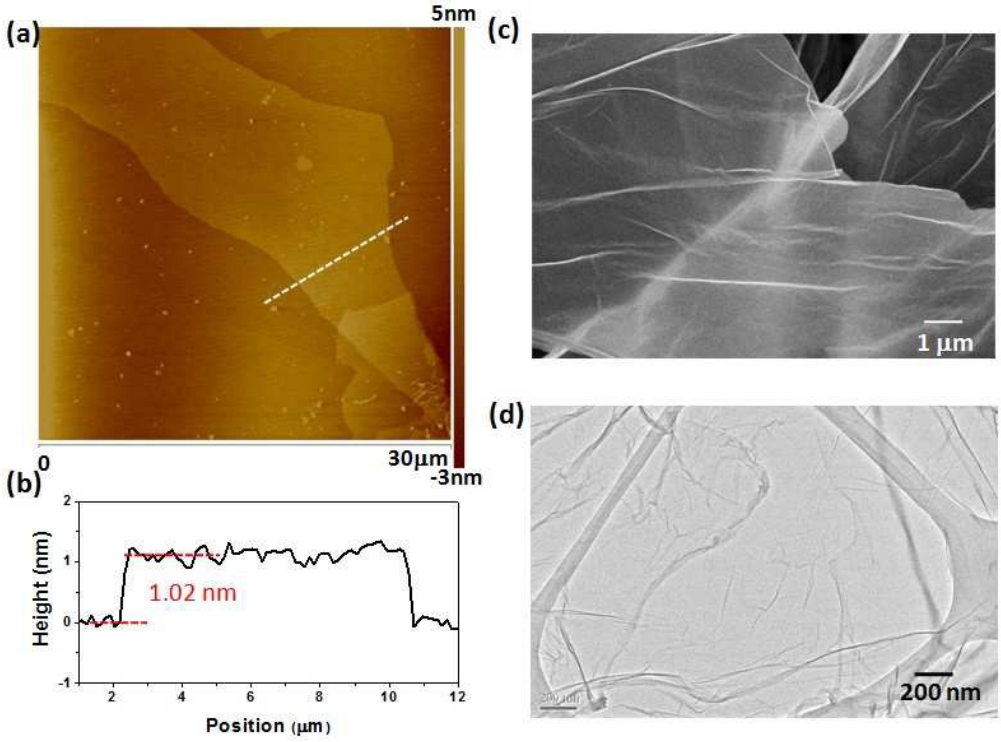

Figure 1. (a)Typical AFM images of the GO sheet. (b) The corresponding height profile for the graphene sheet in (a), indicating that the sheet is approximately 1.76 nm in thickness. (c) SEM image of the surface morphology of the graphene sheets. (d) TEM image of a graphene sheet, showing the wrinkles over the surface of the sheet.

RSC Advances Accepted Manuscript

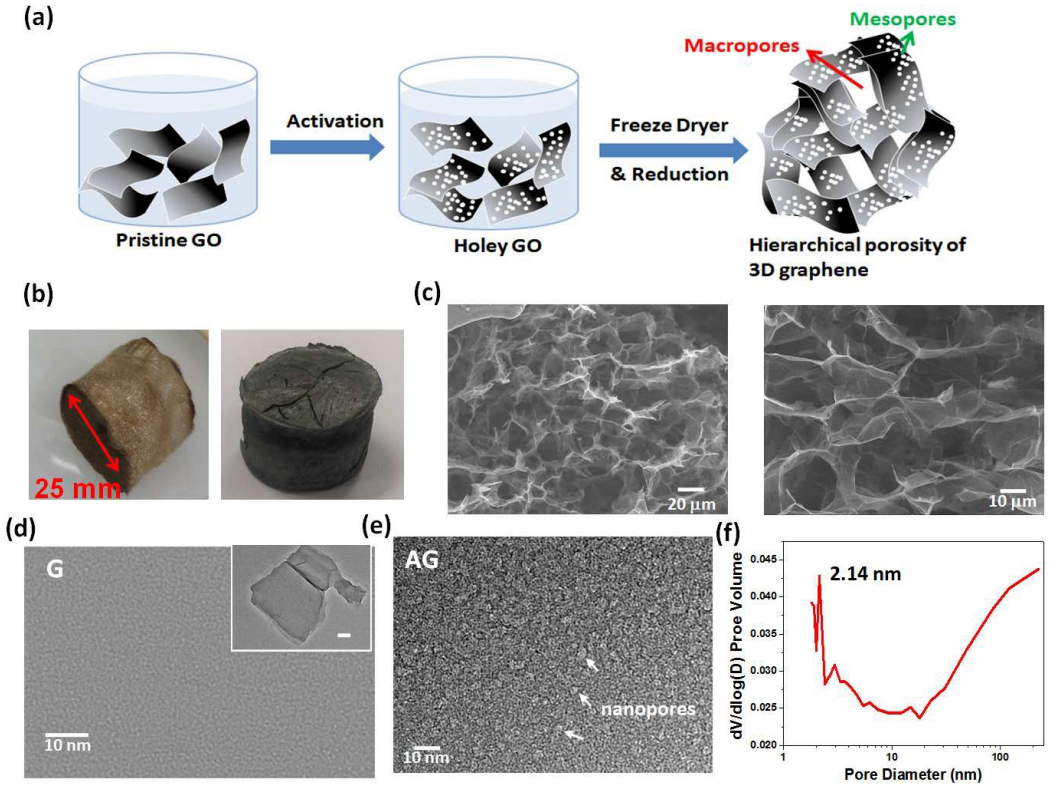

Figure 2.(a) The schematic illustration of the procedures to construct 3D monolithic self-assembled nanoporous graphene. (b) The photo images for the as-prepared 3D graphene foam via freeze-drying(left) and after thermal reduction(right). (c) The low- and high-magnification SEM images of the 3D graphene in (b).(d) The HRTEM image of pristine GO; the inset shows a low magnification image(scale bar is 100 nm).(e) The nanoporous graphene after acid activation, where the white arrows indicate the nanopores on the sheet surface. (f) The pore size distribution of nanoporous graphene after activation, which was characterized by the N_2 adsorption–desorption isotherms analysis.

RSC Advances Accepted Manuscript

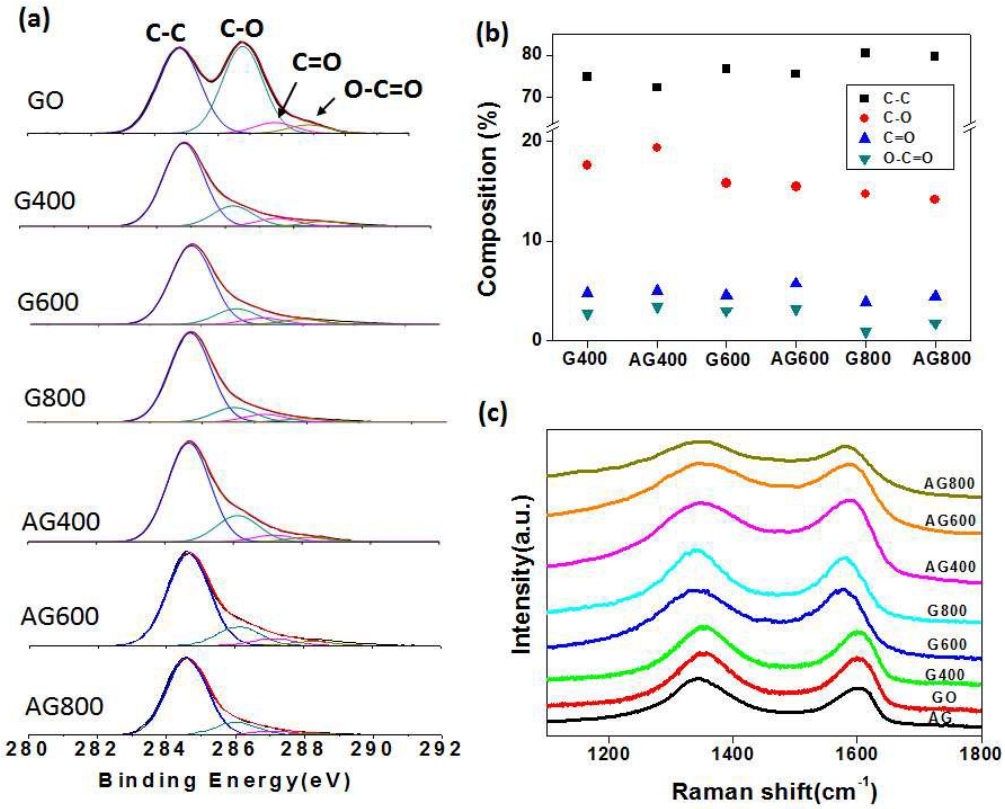

Figure 3.(a)The deconvoluted C1s XPS spectra of GO, thermally reduced GO(G400~G800), and activated GO followed by thermal reduction(AG400~AG800).(b) The compositions of C bonding states, including C-C, C-O,C=O, and O-C=O, in various samples, obtained by the integrated peak areas from the C1s spectra in (a).(c) The corresponding Raman spectra of GO, G and AG samples.

RSC Advances Accepted Manuscript

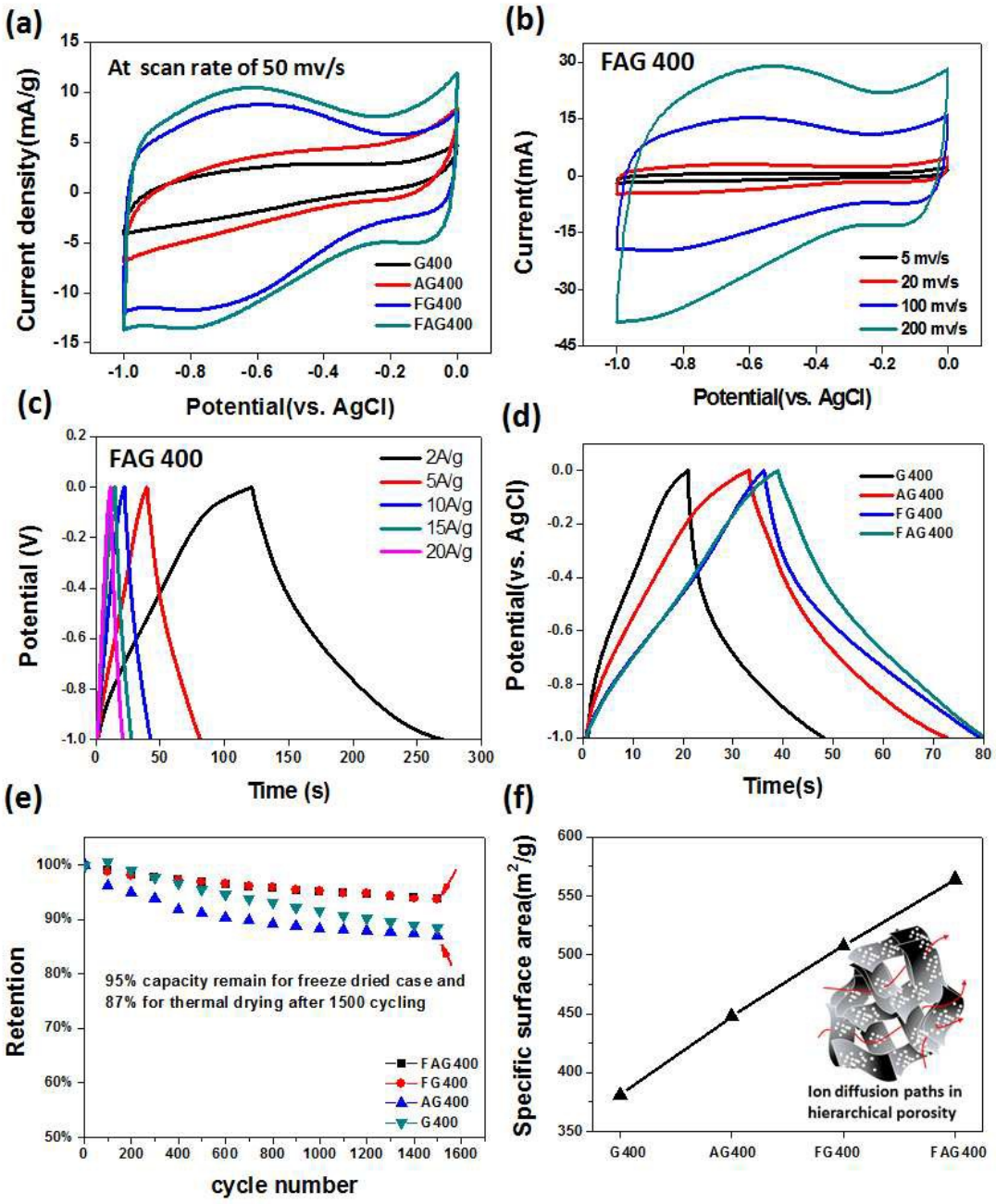

Figure 4. The electrochemical performances of various structured graphene supercapacitors in 6 M KOH aqueous solution. (a) The compiled CV curves at a scan rate of 50 mV/s for various structured graphene samples.(b)The typical CV curve for sample FAG 400 at various scan rates. (c) The corresponding GCD curves of FAG 400

RSC Advances Accepted Manuscript

performed at different current densities. (d) The comparison of GCD curves at current density of 5A/g for FG400 and FAG 400. The raising and decline branch represent the charge and discharge steps, respectively (e) Cycling stability tests for various structured graphene samples at a scan rate of 200 mV/s. (f) The plots reveal the SSA on various graphene electrodes. The inset shows an illustration indicating the creation of many ion permeation paths for the 3D structure self-assembled holey graphene(FAG 400).

RSC Advances Accepted Manuscript

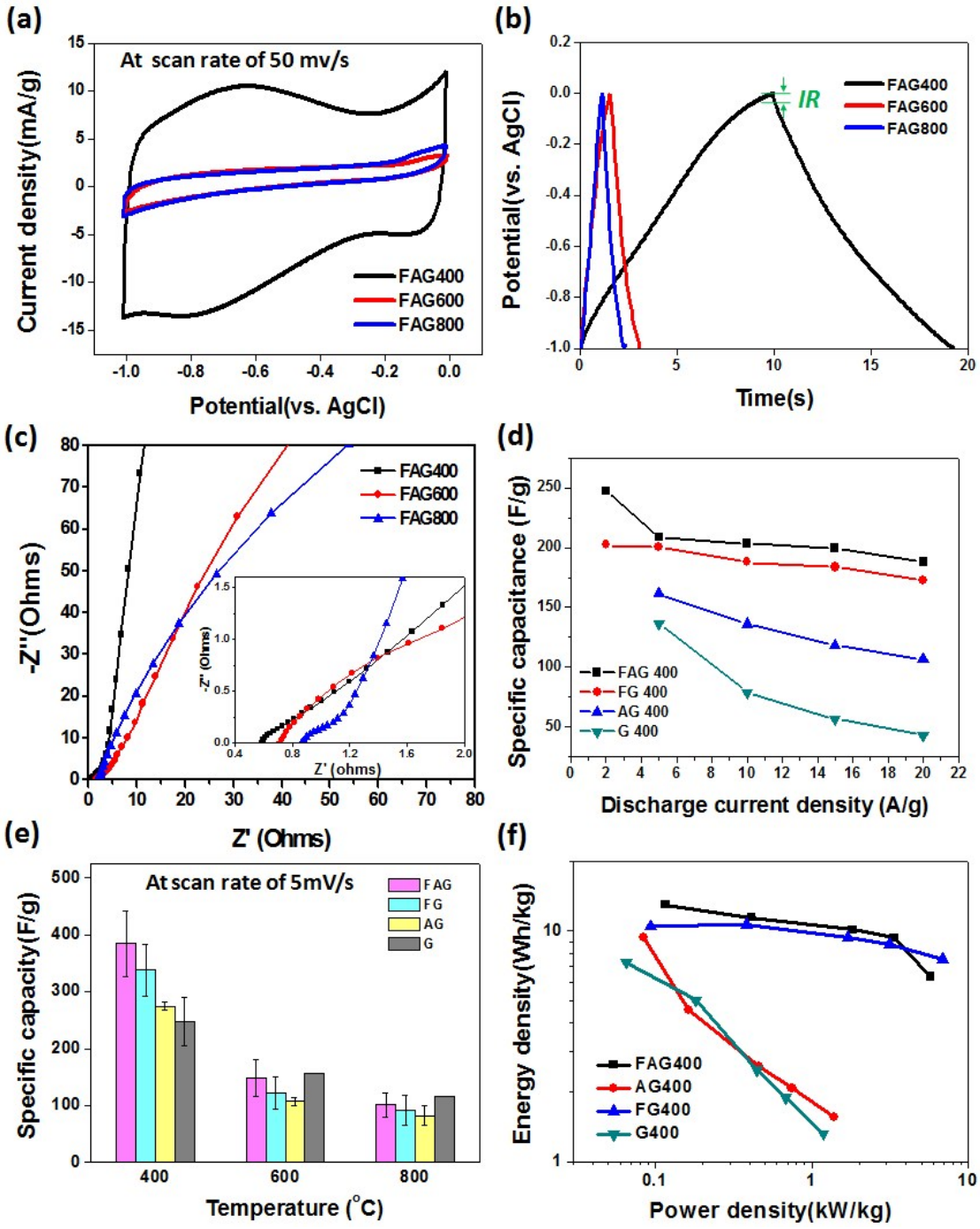

Figure 5. The electrochemical performances of the graphene electrode under various degrees of oxidized functionalization. (a) The CV curves for the FAG sample under different reduction temperatures and (b) the corresponding GCD curves measured at current density of 20A/g. The IR drop is derived from the discharge branch. (c) The

RSC Advances Accepted Manuscript

Nyquist plot for the FAG samples(inset shows the high-frequency region). (d) The rate capacitances of the FAG samples at various current densities. (e) The compiled statistical analysis on the specific capacitance for all the graphene-based electrodes studied here. (f) The Ragone plot of the power density versus the energy density for symmetric supercapacitors with different graphene electrodes.

RSC Advances Accepted Manuscript

Reference

1. R. Raccichini, A. Varzi, S. Passerini and B. Scrosati, *Nature Materials*, 2015, **14**, 271-279.
2. O. A. Vargas C, A. Caballero and J. Morales, *Nanoscale*, 2012, **4**, 2083-2092.
3. J. Hassoun, F. Bonaccorso, M. Agostini, M. Angelucci, M. G. Betti, R. Cingolani, M. Gemmi, C. Mariani, S. Panero, V. Pellegrini and B. Scrosati, *Nano Letters*, 2014, **14**, 4901-4906.
4. J. Zhu, D. Yang, Z. Yin, Q. Yan and H. Zhang, *Small*, 2014, **10**, 3480-3498.
5. C. Xu, B. Xu, Y. Gu, Z. Xiong, J. Sun and X. S. Zhao, *Energy & Environmental Science*, 2013, **6**, 1388-1414.
6. A. L. Ivanovskii, *Russian Chemical Reviews*, 2012, **81**, 571-605.
7. J. Chen, C. Li and G. Shi, *Journal of Physical Chemistry Letters*, 2013, **4**, 1244-1253.
8. P. Simon and Y. Gogotsi, *Nature Materials*, 2008, **7**, 845-854.
9. M. Inagaki, H. Konno and O. Tanaike, *Journal of Power Sources*, 2010, **195**, 7880-7903.
10. Y. Sun, Q. Wu and G. Shi, *Energy & Environmental Science*, 2011, **4**, 1113-1132.
11. Y. Zhu, S. Murali, M. D. Stoller, K. J. Ganesh, W. Cai, P. J. Ferreira, A. Pirkle, R. M. Wallace, K. A. Cychosz, M. Thommes, D. Su, E. A. Stach and R. S. Ruoff, *Science*, 2011, **332**, 1537-1541.
12. J. Maier, *Nature Materials*, 2005, **4**, 805-815.
13. Z. Bo, W. Zhu, W. Ma, Z. Wen, X. Shuai, J. Chen, J. Yan, Z. Wang, K. Cen and X. Feng, *Advanced Materials*, 2013, **25**, 5799-+.
14. X. Xiao, P. Liu, J. S. Wang, M. W. Verbrugge and M. P. Balogh, *Electrochemistry Communications*, 2011, **13**, 209-212.
15. S. M. Jung, D. L. Mafra, C.-T. Lin, H. Y. Jung and J. Kong, *Nanoscale*, 2015, **7**, 4386-4393.

16. H.-P. Cong, X.-C. Ren, P. Wang and S.-H. Yu, *Acs Nano*, 2012, **6**, 2693-2703.
17. H. Hu, Z. Zhao, W. Wan, Y. Gogotsi and J. Qiu, *Advanced Materials*, 2013, **25**, 2219-2223.
18. Z. Chen, W. Ren, L. Gao, B. Liu, S. Pei and H.-M. Cheng, *Nature Materials*, 2011, **10**, 424-428.
19. Y. Xu, K. Sheng, C. Li and G. Shi, *Acs Nano*, 2010, **4**, 4324-4330.
20. H. Bi, X. Xie, K. Yin, Y. Zhou, S. Wan, L. He, F. Xu, F. Banhart, L. Sun and R. S. Ruoff, *Advanced Functional Materials*, 2012, **22**, 4421-4425.
21. Z. Xu, Y. Zhang, P. Li and C. Gao, *Acs Nano*, 2012, **6**, 7103-7113.
22. L. Qiu, J. Z. Liu, S. L. Y. Chang, Y. Wu and D. Li, *Nature Communications*, 2012, **3**.
23. B. G. Choi, M. Yang, W. H. Hong, J. W. Choi and Y. S. Huh, *Acs Nano*, 2012, **6**, 4020-4028.
24. S. M. Jung, H. Y. Jung, M. S. Dresselhaus, Y. J. Jung and J. Kong, *Scientific Reports*, 2013, **3**.
25. Y. Xu, C.-Y. Chen, Z. Zhao, Z. Lin, C. Lee, X. Xu, C. Wang, Y. Huang, M. I. Shakir and X. Duan, *Nano Letters*, 2015, **15**, 4605-4610.
26. S. Ye, J. Feng and P. Wu, *ACS Applied Materials & Interfaces*, 2013, **5**, 7122-7129.
27. Y. Tao, X. Xie, W. Lv, D.-M. Tang, D. Kong, Z. Huang, H. Nishihara, T. Ishii, B. Li, D. Golberg, F. Kang, T. Kyotani and Q.-H. Yang, *Scientific Reports*, 2013, **3**.
28. X. Zhu, P. Zhang, S. Xu, X. Yan and Q. Xue, *Acs Applied Materials & Interfaces*, 2014, **6**, 11665-11674.
29. L. Zhang and G. Shi, *Journal of Physical Chemistry C*, 2011, **115**, 17206-17212.
30. Y. G. Zhu, Y. Wang, Y. Shi, Z. X. Huang, L. Fu and H. Y. Yang, *Advanced Energy Materials*, 2014, **4**.
31. J. Wang and S. Kaskel, *Journal of Materials Chemistry*, 2012, **22**, 23710-23725.
32. L. Qie, W. Chen, H. Xu, X. Xiong, Y. Jiang, F. Zou, X. Hu, Y. Xin, Z. Zhang and Y. Huang, *Energy & Environmental Science*, 2013, **6**, 2497-2504.
33. L. Zhang, F. Zhang, X. Yang, G. Long, Y. Wu, T. Zhang, K. Leng, Y. Huang, Y. Ma, A. Yu and Y. Chen, *Scientific Reports*, 2013, **3**.
34. X. Zhao, C. M. Hayner, M. C. Kung and H. H. Kung, *Acs Nano*, 2011, **5**, 8739-8749.
35. F. Hennrich, R. Krupke, K. Arnold, J. A. Rojas Stütz, S. Lebedkin, T. Koch, T. Schimmel and M. M. Kappes, *The Journal of Physical Chemistry B*, 2007, **111**, 1932-1937.
36. S. Wang, L. A. l. Tang, Q. Bao, M. Lin, S. Deng, B. M. Goh and K. P. Loh, *Journal of the American Chemical Society*, 2009, **131**, 16832-16837.
37. C.-Y. Su, Y. Xu, W. Zhang, J. Zhao, A. Liu, X. Tang, C.-H. Tsai, Y. Huang and L.-J. Li, *ACS Nano*, 2010, **4**, 5285-5292.
38. C.-Y. Su, Y. Xu, W. Zhang, J. Zhao, X. Tang, C.-H. Tsai and L.-J. Li, *Chemistry of Materials*, 2009, **21**, 5674-5680.

RSC Advances Accepted Manuscript

39. B. Zhao, P. Liu, Y. Jiang, D. Pan, H. Tao, J. Song, T. Fang and W. Xu, *Journal of Power Sources*, 2012, **198**, 423-427.
40. Q. Du, M. Zheng, L. Zhang, Y. Wang, J. Chen, L. Xue, W. Dai, G. Ji and J. Cao, *Electrochimica Acta*, 2010, **55**, 3897-3903.
41. C.-M. Chen, Q. Zhang, M.-G. Yang, C.-H. Huang, Y.-G. Yang and M.-Z. Wang, *Carbon*, 2012, **50**, 3572-3584.
42. C. Niu, E. K. Sichel, R. Hoch, D. Moy and H. Tennent, *Applied Physics Letters*, 1997, **70**, 1480-1482.
43. M. Beidaghi and C. Wang, *Advanced Functional Materials*, 2012, **22**, 4501-4510.
44. D. C. Marcano, D. V. Kosynkin, J. M. Berlin, A. Sinitskii, Z. Sun, A. Slesarev, L. B. Alemany, W. Lu and J. M. Tour, *ACS Nano*, 2010, **4**, 4806-4814.
45. M. J. McAllister, J.-L. Li, D. H. Adamson, H. C. Schniepp, A. A. Abdala, J. Liu, M. Herrera-Alonso, D. L. Milius, R. Car, R. K. Prud'homme and I. A. Aksay, *Chemistry of Materials*, 2007, **19**, 4396-4404.

RSC Advances Accepted Manuscript